

Model-based control of cardiac alternans in Purkinje fibers

Alejandro Garzón and Roman O. Grigoriev

School of Physics, Georgia Institute of Technology, Atlanta, Georgia 30332-0430, USA

Flavio H. Fenton

Department of Biomedical Sciences, Cornell University, Ithaca, New York 14853, USA

(Received 25 February 2010; revised manuscript received 12 August 2011; published 21 October 2011)

This paper describes a systematic approach to suppressing cardiac alternans in simulated Purkinje fibers using localized current injections. We investigate the controllability and observability of the periodically paced Noble model for different locations of the recording and control electrodes. In particular, we show that the loss of controllability causes the failure of the control approach introduced by Echebarria and Karma [Chaos **12**, 923 (2002)] for longer fiber lengths. Furthermore, we explain how the optimal locations for the recording and control electrodes and the timing of the feedback current can be selected, accounting for both linear and nonlinear effects, effectively doubling the length of fibers that can be controlled with previous methods.

DOI: [10.1103/PhysRevE.84.041927](https://doi.org/10.1103/PhysRevE.84.041927)

PACS number(s): 87.19.Hh, 05.45.Gg, 02.30.Yy

I. INTRODUCTION

When excitable cardiac tissue is electrically paced at a sufficiently high rate, the duration of excitation (or action potential duration, APD) can alternate from beat to beat [1,2] despite a fixed stimulation period. This rhythm, known as electrical alternans or 2:2, has been identified [3–5] as an early stage in a sequence of increasingly complex instabilities leading to the lethal type of arrhythmia known as ventricular fibrillation (VF) [6]. Hence, suppression of alternans can be considered as a way of preventing VF.

To date, the vast majority of feedback control approaches aimed to suppress alternans in cardiac tissue by adjusting the timing of the electrical pacing stimuli based on the difference between the two most recent APDs. This approach, which we refer to here as the pacing interval adjustment (PIA) method, is a particular implementation of the empiric time-delay autosynchronization control of Pyragas [7]. The earliest experimental attempt to implement PIA in cardiac tissue is due to Hall and Gauthier, who managed to suppress alternans in small (well below 1 cm) patches of frog heart muscle tissue [8]. While PIA control has the benefit that no model of the dynamics is required, it also has limitations: Alternans are suppressed only in a small (~ 1 cm) neighborhood of the pacing electrode.

Since that pioneering study most of the research on feedback control of alternans has concentrated on a specific type of cardiac tissue, Purkinje fiber, which conducts the electrical excitation from the atria to the ventricles. The relative simplicity of this, effectively one-dimensional, excitable tissue makes it an ideal candidate for both experimental and theoretical studies. The first theoretical investigation of PIA in Purkinje fibers is due to Echebarria and Karma [9], who used numerical simulations of the Noble model to show that alternans can be suppressed in fibers no longer than ~ 1 cm. This theoretic prediction was verified experimentally by Christini *et al.* [10]. Studies of other models of cardiac dynamics also find a limit on the fiber length that can be controlled by a single electrode [11].

Echebarria and Karma should also be credited with uncovering some of the dynamical mechanisms which limit the size of tissue that can be successfully controlled. Their theoretical

analysis, based on the amplitude equation formalism, showed that PIA feedback affects only the excitation mode with the lowest spatial frequency, which is destabilized first when the alternans appear. Higher-frequency modes cannot be suppressed and, as those become unstable for longer fibers and shorter pacing intervals, the tissue develops alternans even in the presence of feedback.

The main contribution of the present paper is to extend this analysis by placing the control problem, which heretofore was primarily based on an empirical approach, on a solid theoretical foundation. This foundation will allow us to understand not only why the PIA control fails, but also how the feedback control should be designed and implemented to avoid this size limitation. In particular, using model-based control, it will address a number of experimentally critical issues: (i) How many electrodes are needed to control a tissue of a given size? (ii) Where should these electrodes be located relative to the pacing electrode? (iii) If impulsive feedback is used, what is the optimal timing? (iv) How should the feedback strength be computed (instead of being determined empirically, which is the case for PIA)?

We will start by describing the mathematical model in Sec. II. Section III is devoted to a numerical investigation of the dynamical regimes produced by the model with and without PIA. A stability analysis of the model is performed in Sec. IV, followed by the description of the proposed model-based-control approach in Sec. V. Finally, our results and conclusions are presented in Sec. VI.

II. MODEL EQUATIONS

In our paper we chose to use the Noble model of ionic dynamics [12], which describes the evolution of three gating variables a , b , c , and the transmembrane voltage V . Using a nondimensionalized variable

$$u = \frac{V - V_{\text{off}}}{V_{\text{sc}}}, \quad (1)$$

where V is expressed in mV, $V_{\text{off}} = -84$ mV, and $V_{\text{sc}} = 124$ mV (chosen so that u takes values mostly in the range

[0, 1]), the Noble model for a single cell can be written in a compact vector form

$$\dot{\mathbf{z}} = F(\mathbf{z}), \quad (2)$$

where $\mathbf{z} = [u, a, b, c]^\dagger$. All parameter values are chosen as in Ref. [9].

While it can be argued that the Noble model is not the most accurate model of a Purkinje cell, since it lacks many features of more complex cell models, currently, to the best of our knowledge, there are no other mathematical models of Purkinje cells or fibers that produce alternans. For example, the more complicated updated version of this model (the 1985 Di Francesco-Noble), which includes more detailed calcium dynamics, fails to produce alternans [13]. Even the two most recently developed Purkinje models [14,15] do not show alternans. The Noble model not only captures the essential dynamics, it also provides an opportunity for direct comparison of our results with previous studies [9]. Furthermore, it should be pointed out that our approach, the main results, and conclusion are very general and by no means limited to a particular ionic model. Moreover, the whole approach can be easily generalized to two- or three-dimensional tissue (e.g., atria and ventricles).

A paced Purkinje fiber is modeled by a system of partial differential equations, which generalizes the single-cell model (2),

$$\partial_t \mathbf{z} = D \partial_x^2 \mathbf{z} + F(\mathbf{z}) - \hat{\mathbf{u}} j, \quad (3)$$

where $D = D_e \hat{\mathbf{u}} \hat{\mathbf{u}}^\dagger$ describes electric coupling between cells and $\hat{\mathbf{u}} = [1, 0, 0, 0]^\dagger$. The value of the diffusion constant D_e was chosen as in Ref. [9]. Vanishing-electric-current boundary conditions are imposed at both ends of the fiber $\partial_x u|_{x=0,L} = 0$.

The last term in Eq. (3) represents the current density injected by one or more electrodes for pacing and/or control. For instance, the pacing current $I_p(t)$ applied by a single electrode can be described by

$$j(x, t) = I_p(t) g(x - x_p), \quad (4)$$

where $g(x - x_p)$ describes the polarization profile produced by an electrode placed at location $x = x_p$. In this study we choose $g(x)$ as a normalized Gaussian of width $\sigma = 0.1$ cm and $x_p = 0.25$ cm. The pacing current consists of a periodic sequence of square pulses $I_p(t) = I_p^0(t \bmod T)$, where

$$I_p^0(t) = \begin{cases} I_0, & 0 < t < \Delta T_p, \\ 0, & \Delta T_p < t < T, \end{cases} \quad (5)$$

T is a constant pacing period, and the pulse duration ΔT_p was chosen equal to 5 ms following Ref. [9]. The beginning of the n th pulse is then given by $t_n = nT$. Each pacing stimulus produces a traveling wave of action potential that propagates from the pacing electrode toward both ends of the fiber.

The dynamics of the paced fiber can be conveniently represented in terms of the action potential duration (APD) at a given location x defined as the time that lapses between the instant u surpasses a threshold value u_{th} during depolarization and the instant it falls below that value during repolarization (Fig. 1). The APD at a particular position x for a particular pacing stimulus n will be indicated as $APD_n(x)$ here. When a fiber is paced over a long-time interval, it is observed that after

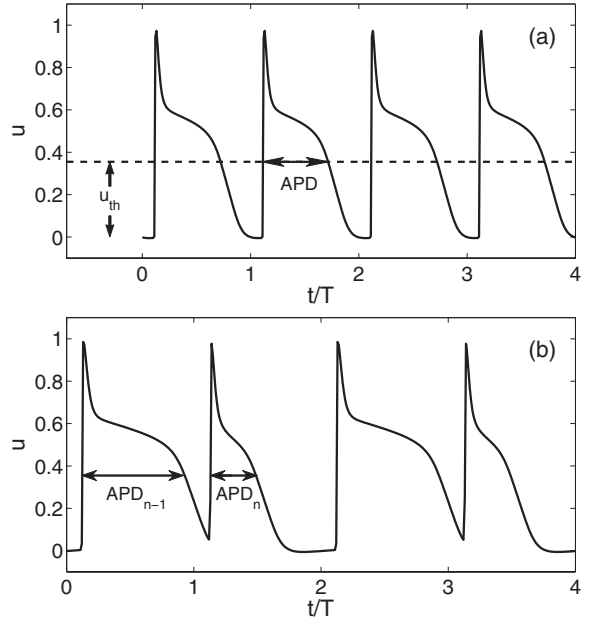


FIG. 1. Transmembrane potential $u(x, t)$ at $x = 1$ cm for a fiber of length $L = 5$ cm: (a) normal rhythm at $T = 270$ ms, (b) alternans at $T = 250$ ms.

a transient period during which the dynamics depends on the initial conditions, $APD_n(x)$ approaches an asymptotic regime. When T is bigger than some critical value T_c , $APD_n(x) = APD(x)$ [Fig. 1(a)]. This is the normal (or 1:1) rhythm. When T is less than T_c , $APD_n(x)$ alternates between long and short from beat to beat [Fig. 1(b)]. In particular, for the Noble model, while $APD_{n+1}(x) \neq APD_n(x)$ for most x values, $APD_{n+2}(x) = APD_n(x)$ for all x . This second regime is known as the state of alternans (or 2:2 rhythm).

The onset of the state of alternans when the pacing rate is increased is a well-established result demonstrated by both experiments and simulations [2–4,16–19]. Alternans could be *concordant*, if the difference $APD_{n+1}(x) - APD_n(x)$ has the same sign for all x or *discordant* if it does not.

The current given by Eq. (4) can be injected experimentally in cardiac tissue by a microelectrode, and while it is easier to excite tissue to prolong an action potential, it is also possible to deexcite tissue, thereby advancing repolarization by prematurely decreasing an action potential through current application, as has been shown in Purkinje fibers by Nakaya *et al.* [20].

III. NON-MODEL-BASED CONTROL

Echebarria and Karma [9] achieved success in suppressing alternans in the Noble model for small-size fibers by adjusting the pacing interval

$$t_{n+1} - t_n = T + \Delta T^n, \quad (6)$$

based on the difference between the two most recent APD values recorded by the pacing electrode

$$\Delta T^n = \frac{\gamma}{2} [APD_n(x_p) - APD_{n-1}(x_p)], \quad (7)$$

where γ is an empirically chosen constant. Throughout this paper we will refer to this control approach as pacing interval adjustment (PIA).

The results reported in Ref. [9] set the benchmark against which the control procedures for the open fiber that we propose in this paper are measured. As a validation for our numerical algorithms, we reproduced the results of Echebarria and Karma. We explored the performance of PIA for different pacing intervals using the protocol from Ref. [9]: For a given length, starting from a period of $T = 280$ ms where alternans are absent, we decreased the pacing interval in steps of 5 ms and applied 200 stimuli for each value of T . This procedure was repeated for fibers of different lengths. We note that while in Ref. [9] the pacing electrode is located at the left end of the fiber ($x_p = 0$), we used $x_p = 0.25$ cm. The location $x_p = 0$ was avoided on the assumption that for some experimental settings it might be difficult to achieve proper electrical contact between the end of the fiber and the electrode. As we show below, this difference in x_p does not introduce any significant discrepancy between our results and those of Ref. [9].

In the uncontrolled case, which corresponds to setting $\gamma = 0$ in Eq. (7), presented in the top panel of Fig. 2, the onset of alternans occurs at roughly the same pacing period ($265 \text{ ms} < T_c < 270 \text{ ms}$) regardless of the length of the fiber. Once the normal rhythm is destabilized for $T < T_c$, we find the same dynamical regimes as in Ref. [9], but the regions in the (L, T) parameter space where those regimes can be found differ between the two studies. This is especially noticeable for the conduction block regime, which occurs at faster pacing rates, for which the pacing current fails to produce a traveling action potential; in our study it occurs at a longer pacing interval (~ 220 ms) compared with Ref. [9] (180–195 ms). This may be a consequence of insufficiently accurate time discretization employed in the earlier study: Echebarria and Karma used the time step $\Delta t = 0.05$ ms in the numerical integration of the evolution equation, while the present study used a smaller time step $\Delta t = 0.01$ ms. However, the discrepancy could also be due to the bistability present at some parameter values, with one of two stable states selected by initial conditions.

In both studies, PIA is able to suppress alternans (solid circles) for either short fibers or (in general) low pacing rates. Similar to Ref. [9], we find (bottom panel of Fig. 2) that for longer fibers and higher pacing rates the alternations of the APD are greatly reduced at the pacing location but not away from it. A state develops in which the amplitude of APD oscillations increases with the distance from the pacing site (referred to as the “first harmonic standing wave”). A further increase of the pacing rate or fiber length produces traveling discordant alternans. At even faster pacing rates and greater fiber lengths conduction block is observed. The two studies are in reasonable agreement regarding the success of PIA control: Normal rhythm can be maintained for all pacing rates, only in fibers somewhat shorter than 1 cm. The remainder of this paper is devoted to explaining why this limitation arises and investigates how it can be circumvented.

IV. LINEAR STABILITY ANALYSIS

The analysis presented in this paper is based on an approach similar to that of Refs. [21] and [22]. As in those

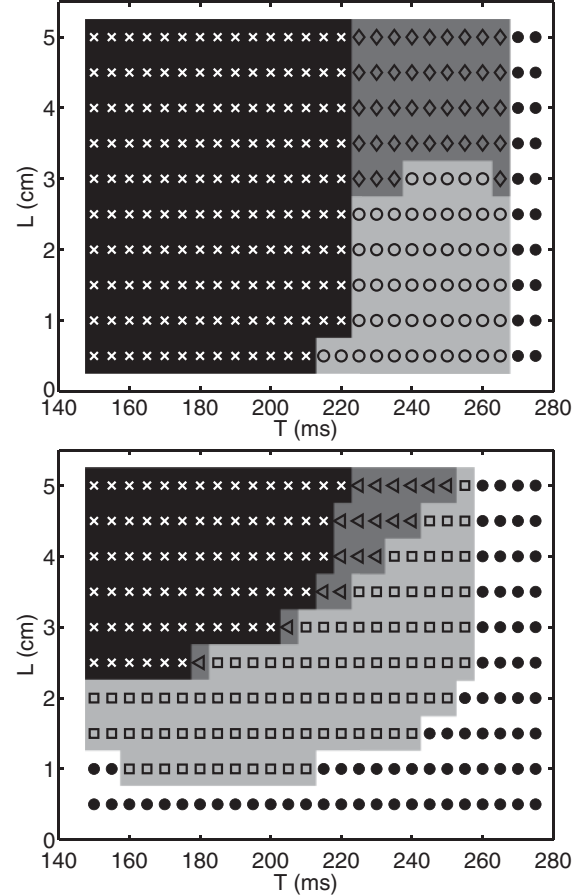


FIG. 2. Dynamical regimes of the paced fiber in the absence of control ($\gamma = 0$, top) and with PIA control ($\gamma = 1/2$, bottom): normal rhythm (solid circles), concordant alternans (open circles), discordant stationary alternans (diamonds), first harmonic standing wave (squares), traveling discordant alternans (triangles), and conduction block (crosses). Levels of gray were added to aid visualization.

studies, we linearize the evolution equation (3) about the time-periodic solution representing normal rhythm and perform a Galerkin projection of the resulting (linear) equation onto the eigenfunctions of the evolution operator. In those previous studies the rotational or translational symmetry of the system afforded a significant simplification: Normal rhythm could be represented as a rotating or translating steady state by an appropriate change of reference frame. No such reference frame transformation is possible for the open fiber, so one is forced to perform a linear stability (or Floquet) analysis of a time-dependent solution.

The model (3) and (4) possesses a time-periodic solution $\mathbf{z}_0(x, t)$, corresponding to normal rhythm with the period T determined by that of the pacing current. Let $G(\mathbf{z}; T, 0)$ denote the time evolution operator

$$\mathbf{z}(x, T) = G[\mathbf{z}(x, 0); T, 0]. \quad (8)$$

Since $\mathbf{z}_0(x, 0)$ is a periodic orbit, it is a fixed point of $G(\mathbf{z}; T, 0)$,

$$\mathbf{z}_0 = G[\mathbf{z}_0; T, 0]. \quad (9)$$

We solved (9) using a matrix-free Newton-Krylov method [23] (see Appendix A1 for details) combined with generalized

minimal residual method (GMRES). The latter is implemented by the MATLAB (Mathworks, Inc.) routine gmres.

In order to determine the stability of normal rhythm we consider the dynamics of small perturbations $\delta\mathbf{z} = \mathbf{z} - \mathbf{z}_0$, governed by the linearization of (3)

$$\partial_t \delta\mathbf{z} = J_{\mathcal{N}}(t) \delta\mathbf{z} - \hat{\mathbf{u}} j_c, \quad (10)$$

where $J_{\mathcal{N}}(t) = D\partial_x^2 + J_F(t)$ with $J_F(t) \equiv DF/D\mathbf{z}|_{\mathbf{z}_0(x,t)}$ —the Jacobian of $F(\mathbf{z})$ evaluated along the periodic orbit $\mathbf{z}_0(x,t)$. The current density $j = j_p + j_c$ now includes both the pacing current j_p defined by (4) and the feedback current j_c , to be computed later.

Considerable simplification can be achieved by introducing a stroboscopic section $t'_n = \tau + nT$, with $n = 1, 2, \dots$ and $0 \leq \tau < T$, which reduces the time-dependent problem (10) to a map:

$$\begin{aligned} \delta\mathbf{z}(x, t'_{n+1}) &= U(\tau + T, \tau) \delta\mathbf{z}(x, t'_n) \\ &\quad - \int_0^T U(\tau + T, \tau + t) \hat{\mathbf{u}} j_c^n(x, t) dt, \end{aligned} \quad (11)$$

where $U(t_f, t_i)$ is the linear time evolution operator of (10) in the absence of control ($j_c = 0$) and $j_c^n(x, t) = j_c(x, t'_n + t)$, for $t \in [0, T]$. In deriving (11) we used the fact that due to the time periodicity of $J_{\mathcal{N}}(t)$, $U(t_f, t_i)$ is also time periodic with period T ,

$$U(t_f + T, t_i + T) = U(t_f, t_i). \quad (12)$$

Note that in introducing the stroboscopic section we allowed the freedom to change its temporal phase relative to the pacing stimulus, which corresponds to $\tau = 0$. This will later allow us to investigate how the dynamics responds to current injections applied not only at different positions along the fiber, but also with different time delays relative to the pacing stimulus.

In the absence of control the stroboscopic map (11) takes a very simple form

$$\delta\mathbf{z}(x, t'_{n+1}) = U(\tau + T, \tau) \delta\mathbf{z}(x, t'_n). \quad (13)$$

The stability of \mathbf{z}_0 is determined by the eigenvalues λ_i of this map:

$$U(\tau + T, \tau) \mathbf{e}_i(x, \tau) = \lambda_i \mathbf{e}_i(x, \tau), \quad (14)$$

where \mathbf{e}_i are the corresponding eigenfunctions. Here we assume the eigenvalues to be ordered such that $|\lambda_1| \geq |\lambda_2| \geq \dots$. It can be shown that λ_i are independent of τ and that the (right) eigenfunctions of $U(\tau + T, \tau)$ for arbitrary τ can be computed as

$$\mathbf{e}_i(x, \tau) = U(\tau, 0) \mathbf{e}_i(x, 0) \quad (15)$$

using the eigenfunctions for $\tau = 0$ (see Appendix B1).

The spectrum of $U(T, 0)$ was found using the implicitly restarted Arnoldi iteration method [24], implemented by the MATLAB routine eigs. For the sake of efficiency, this method was also applied in its matrix-free form using a routine that calculates the matrix-vector product, in this case $U(T, 0) \delta\mathbf{z}$, instead of the explicit matrix representation of $U(T, 0)$ (see Appendix A2 for details). The number of unstable eigenvalues ($|\lambda_i| > 1$) found for a grid of pairs (L, T) is shown in Fig. 3.

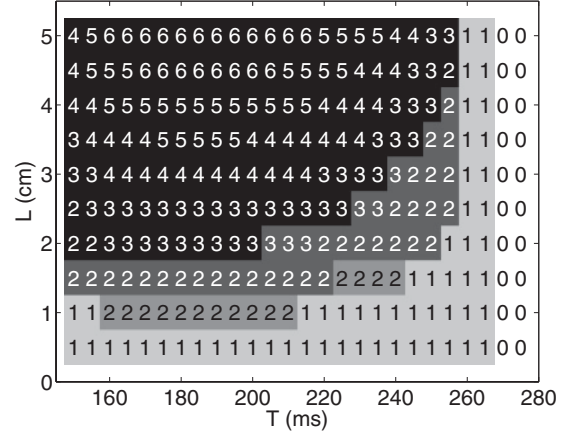


FIG. 3. Stability diagram, showing the number of unstable modes for normal rhythm. White indicates the region in parameter space where normal rhythm is stable. Alternans can be successfully suppressed using PIA control only in the light gray region. Model-based control is successful everywhere in the gray-shaded regions. Feedback is computed using the complete system state in the dark gray region or using local voltage recordings in the medium and light gray regions. All control methods we investigated fail in the black region.

We find that, for the range of L values considered, the normal rhythm \mathbf{z}_0 becomes unstable at $T < T_c$ and alternans develops, which is consistent with the results presented in Fig. 2.

For the range of parameters considered in this paper we found that all eigenvalues of λ_i are negative real numbers. Hence the normal rhythm becomes unstable when an eigenvalue λ_i crosses the unit circle, leading to a period-doubling bifurcation. This is consistent with the fact that the state of alternans is a periodic orbit with a period that is twice that of the pacing current T .

By comparing Fig. 3 with Fig. 2 we find that PIA control succeeds when there is only one unstable mode and fails otherwise. This observation is consistent with the conclusion of Ref. [9] that PIA control can only suppress the mode with the lowest spatial frequency, which happens to be the most unstable one here due to the contribution of the diffusion term $D\partial_x^2 \delta\mathbf{z}$ in (10).

Figure 4 shows the variation of the APD, $\delta A_n(x)$, which corresponds to the three unstable eigenmodes for $L = 2.5$ cm and $T = 220$ ms. The leading mode corresponds to concordant alternans, while the two subleading modes correspond to discordant alternans with one and two nodes, respectively. While the number of nodes is correctly predicted by the analysis in Ref. [9], the precise spatial structure of disturbances is substantially different from the Fourier modes

$$\delta A_n(x) \sim 1 + \alpha_n \cos \frac{\pi(n-1)x}{L}, \quad (16)$$

with $\alpha_n = \text{const}$, predicted by the amplitude equation formalism, highlighting its limitations in describing the dynamics far from onset of the instability.

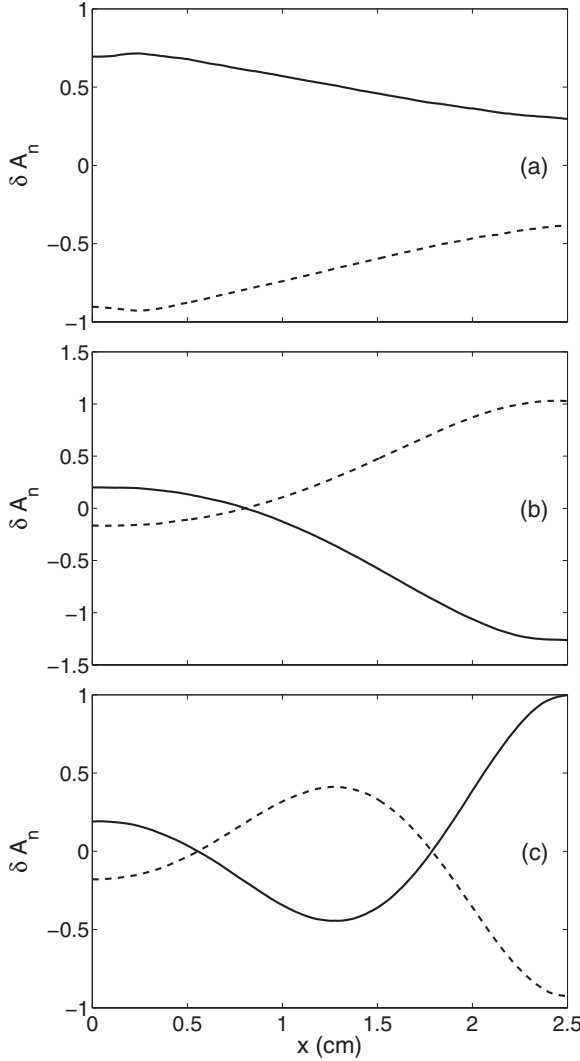


FIG. 4. The perturbation of the APD $\delta A_n(x)$ which corresponds to (a) e_1 , (b) e_2 , and (c) e_3 . The solid and dashed lines correspond to odd and even n , respectively.

V. MODEL-BASED CONTROL

The goal of control is to suppress the transition to alternans by applying feedback, extending the linear stability of the normal rhythm to shorter T . A more convenient description of the dynamics in the presence of feedback can be obtained by projecting (11) onto the basis $\{e_i\}$. This requires the eigenfunctions f_i of the adjoint evolution operator

$$U^\dagger(\tau + T, \tau) f_i(x, \tau) = \lambda_i^* f_i(x, \tau). \quad (17)$$

The adjoint (or left) eigenfunctions $f_i(x, 0)$ can be computed using the matrix-free approach described previously, where the action of the operator $U^\dagger(T, 0)$ is computed by time-discretizing $U(T, 0)$ and evaluating the adjoint of the resulting composition of operators (see Appendix A3 for details). The relationship

$$f_i(x, \tau) = (\lambda_i^*)^{-1} U^\dagger(T, \tau) f_i(x, 0) \quad (18)$$

can then be used to compute the left eigenfunctions for $0 < \tau < T$ (see Appendix B2).

When properly normalized, the left and right eigenfunctions satisfy the orthogonality condition

$$\langle f_i(x, \tau), e_j(x, \tau) \rangle \equiv \int_0^L f_i^*(x, \tau) \cdot e_j(x, \tau) dx = \delta_{ij}, \quad (19)$$

where $\langle \cdot, \cdot \rangle$ denotes the inner product. Therefore, we can expand the perturbation as

$$\delta z(x, t'_n) = \sum_{i=1}^{\infty} \xi_i^n e_i(x, \tau), \quad (20)$$

where

$$\xi_i^n = \langle f_i(x, \tau), \delta z(x, t'_n) \rangle. \quad (21)$$

Substituting (20) into (11) and applying the operation $\langle f_j, \cdot \rangle$ to each side of the resulting equation we obtain

$$\xi_i^{n+1} = \lambda_i \xi_i^n - \left\langle f_i(x, \tau), \int_0^T U(\tau + T, \tau + t) \hat{u} j_c^n(x, t) dt \right\rangle. \quad (22)$$

The choice of the current density j_c^n depends on the number and placement of electrodes used to apply feedback. While experimentally it is possible to pace from the recording sites, in the present paper we will assume there is a single control electrode to enable direct comparison with the PIA approach of Ref. [9], in which case

$$j_c^n(x, t) = I_c^n(t) g(x - x_c), \quad (23)$$

where $I_c^n(t)$ is the control current applied during the n th pacing interval and x_c is the position of the control electrode. For instance, if we split the interval $[t'_n, t'_{n+1}]$ into l subintervals of duration $\delta T = T/l$, following Ref. [22], and assume the current to be constant, $I_c^n(t) = I^{nk}$ on the k th subinterval, (22) reduces to

$$\xi_i^{n+1} = \lambda_i \xi_i^n - \sum_{k=1}^l B_{ik} I^{nk}, \quad (24)$$

where

$$B_{ik} = \left\langle f_i(x, \tau), \int_{(k-1)\delta T}^{k\delta T} U(\tau + T, \tau + t) \hat{u} g(x - x_c) dt \right\rangle. \quad (25)$$

Galerkin truncation involves discarding strongly stable modes ($|\lambda_i| \ll 1$) in order to obtain a low-dimensional map describing the evolution of the unstable and weakly stable modes

$$\xi^{n+1} = A \xi^n - B I^n, \quad (26)$$

where $\xi^n = [\xi_1^n, \xi_2^n, \dots, \xi_m^n]^\dagger$, A is a diagonal matrix with elements $A_{ii} = \lambda_i$, and $I^n = [I^{n1}, I^{n2}, \dots, I^{nl}]^\dagger$.

A variety of standard control-theoretic methods can be invoked to compute the feedback current I^n as a function of the perturbation ξ^n using (26). At the same time, control can be greatly optimized by allowing the feedback current to remain a continuous function of time, which corresponds to choosing a sufficiently large l and imposing no restrictions on I^{nk} . However, in this paper we will limit our attention to the simplest implementation, where only impulsive feedback is considered, $I^{nk} = I^{n1} \delta_{k1}$, in which case the control current

consists of a brief pulse of duration $\delta T \ll T$, so that (25) reduces to

$$\begin{aligned} B_{i1} &\approx \langle \mathbf{f}_i(x, \tau), U(\tau + T, \tau) \delta T \hat{\mathbf{u}} g(x - x_c) \rangle \\ &= \lambda_i \delta T \langle \mathbf{f}_i(x, \tau), \hat{\mathbf{u}} g(x - x_c) \rangle \\ &\approx \lambda_i \delta T f_i^u(x_c, \tau), \end{aligned} \quad (27)$$

where the superscript u denotes the first (voltage) component of \mathbf{f}_i . In the last step we used the fact that $\sigma \ll L$. Defining the total charge $Q^n = I^{n1} \delta T$ injected by the electrode during this brief interval, we find that the stroboscopic map (24) takes the form

$$\xi_i^{n+1} \approx \lambda_i \xi_i^n - \lambda_i f_i^u(x_c, \tau) Q^n. \quad (28)$$

In the limit $\Delta T^n \ll \Delta T_p \ll T$, which corresponds to small deviations from normal rhythm, PIA control can be cast in a very similar form:

$$\xi_i^{n+1} \approx \lambda_i \xi_i^n - \lambda_i (f_i^u(x_p, \Delta T_p) - f_i^u(x_p, 0)) \frac{Q_p}{\Delta T_p} \Delta T^n, \quad (29)$$

where Q_p is the charge delivered by one pacing impulse of duration ΔT_p and ΔT^n was defined in Eq. (7).

A. Controllability

Equations (28) and (29) allow an interesting and important interpretation. When $f_i^u(x_c, \tau) \approx 0$ for some unstable mode i , the feedback has no (or very little) effect on the dynamics of that mode (the mode becomes *uncontrollable*) and the instability cannot be suppressed, regardless of how the current is chosen. On the other hand, the larger $|f_i^u(x_c, \tau)|$ is, the smaller the feedback current can be. The structure of the adjoint eigenfunctions, therefore, determines where the control electrode(s) should be placed and how the timing of the control impulse should be chosen. A similar conclusion was made for spiral waves in a two-dimensional tissue model in Ref. [21].

Using the same electrode for both pacing and control is not only convenient from the experimental perspective, this choice also provides near optimal controllability regardless of

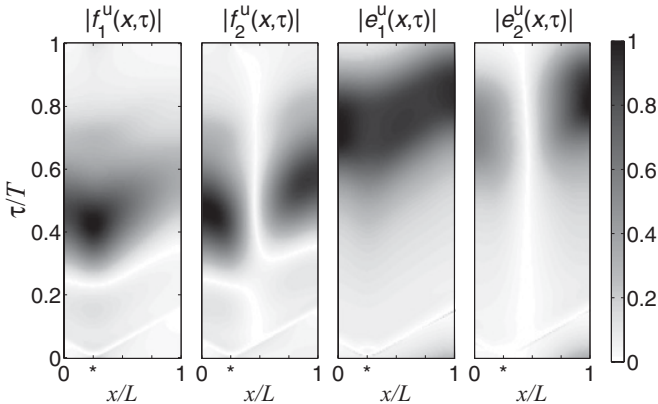


FIG. 5. Controllability and observability of the two unstable modes for $L = 1$ cm and $T = 210$ ms. The star indicates the location of the pacing electrode. The gray scale shows the magnitude of the indicated eigenfunctions.

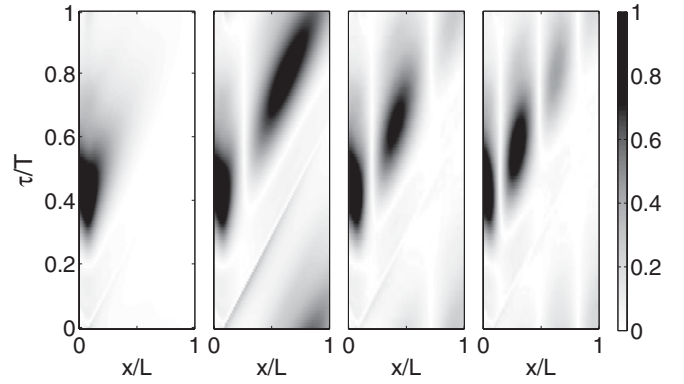


FIG. 6. Controllability $|f_i^u(x, \tau)|$ of the four leading (unstable) modes for $L = 3$ cm and $T = 185$ ms. From left to right, $i = 1, 2, 3, 4$, respectively.

the fiber length. As Figs. 5 and 6 illustrate, $|f_i^u(x_p, \tau)|$ reaches near-maximal values for all unstable modes for both short ($L = 1$ cm) and long ($L = 3$ cm) fibers, such that all unstable modes can be made controllable by an appropriate choice of τ . Therefore, in the remainder of this paper we set $x_c = x_p$.

Experimental considerations do not impose any constraints on the timing of feedback, while controllability requires that the control impulse be delivered much later than the pacing impulse. We discovered that the optimal interval $0.3T \lesssim \tau \lesssim 0.6T$, where $|f_i^u(x_p, \tau)|$ takes nearly maximal values for all unstable modes (hence requiring the smallest control current), is essentially independent of L , as illustrated by a comparison

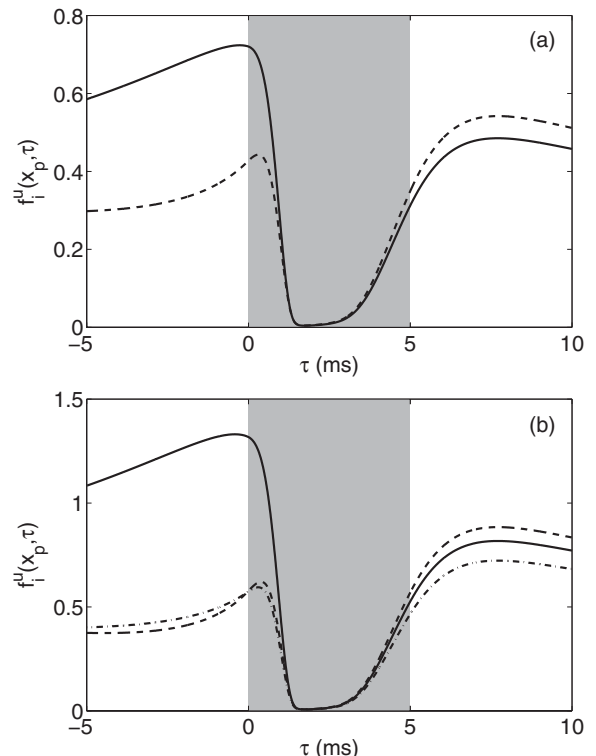


FIG. 7. $f_i^u(x_p, \tau)$ for (a) $L = 1$ cm and (b) $L = 2$ cm. In both cases $T = 210$ ms. Only i values for unstable modes are shown: $i = 1$ (solid line), $i = 2$ (dashed line), $i = 3$ (dotted-dashed line). The gray shade indicates the range $0 < \tau < \Delta T_p$.

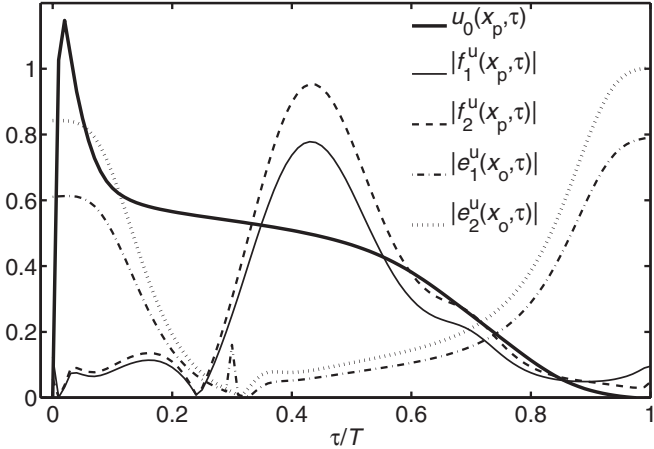


FIG. 8. Controllability and observability of the unstable modes and normal rhythm voltage for $L = 2$ cm, $T = 220$ ms, $x_c = x_p = 0.25$ cm, and $x_o = 1.8$ cm.

of Figs. 5 and 6. Furthermore, as Fig. 8 shows for a 2-cm-long fiber, the optimal timing corresponds to the end of the plateau phase of the action potential. In contrast, for single cells modeled using the canine ventricular myocyte model, the optimal time for feedback was determined to be at the early plateau phase [25].

For PIA, feedback timing does not fall into the optimal range. On the contrary, for every i , $|f_i^u(x_p, \tau)|$ has a deep minimum in the range $0 < \tau < \Delta T_p$, as Fig. 7 shows. As the right-hand side of (29) shows, when feedback is imposed by shifting the timing of the pacing impulse, the magnitude of the difference $\Delta f_i^u \equiv f_i^u(x_p, \Delta T_p) - f_i^u(x_p, 0)$ determines controllability instead of $|f_i^u(x_p, \tau)|$. As Table I shows, $|\Delta f_i^u|$ is of order unity only for $i = 1$ (the leading mode is controllable). All subleading modes are, at best, weakly controllable, indicating that PIA control has virtually no effect on their dynamics and hence is expected to fail. This is in perfect agreement with Ref. [9], which showed that feedback only affects the dynamics of the leading mode.

Model-based control provides a viable alternative to PIA in the region of the (L, T) parameter space characterized by multiple unstable modes. Once x_c and τ have been selected, we can define a vector with components $B'_i = \lambda_i f_i^u(x_c, \tau)$, which recasts the system (28) in the compact form

$$\xi^{n+1} = A\xi^n - B'Q^n. \quad (30)$$

Now the impulsive feedback Q^n stabilizing normal rhythm can be computed using any standard control-theoretic method. Here we use discrete-time linear-quadratic regulator control

TABLE I. The values of $|\Delta f_i^u| = |f_i^u(x_p, \Delta T_p) - f_i^u(x_p, 0)|$ for (a) $L = 1$ cm and (b) $L = 2$ cm. The bold font corresponds to unstable modes. In both cases $T = 210$ ms.

i	1	2	3	4
$ \Delta f_i^u ^{(a)}$	0.4080	0.0780	0.0054	0.0926
$ \Delta f_i^u ^{(b)}$	0.7909	0.0082	0.1086	0.0716

[26] (implemented via the MATLAB routine dlqr) which yields the feedback law

$$Q^n = -K\xi^n, \quad (31)$$

with feedback gain K making the matrix $A + B'K$, and hence the evolution described by the map (30), stable.

B. Observability

In experiment, the mode amplitudes ξ_i^n in Eq. (31) will not be directly accessible. Moreover, despite the advent of optical techniques relying on voltage- or calcium-sensitive dies which can yield spatiotemporal information about more than one state variable, transmembrane voltage recordings from one or more electrodes remain the only practical and reliable way to get information about the system state. One, therefore, has to rely on localized voltage measurements for control purposes, just as most previous studies have done.

Fortunately, state reconstruction is also a standard problem in control theory. The idea is to simulate a numerical model of the experimental system in real time and compare the measurements obtained from experiment with predictions of the model, adjusting the model variables for any discrepancy in the outputs. Such a model is known in control theory as an *observer* or *estimator* [26]. Similar to the PIA implementation in Ref. [9], we will use a single electrode to record the voltage, but will use one measurement per pacing interval in contrast with PIA, which requires continuous measurement of u to determine the APD. This is done to simplify the discussion. Radically more accurate results can be obtained from continuous-time measurements of the voltage.

The output produced by an electrode of finite spatial extent and centered at x_o can be modeled by writing the recorded voltage as

$$v^n = \int g(x - x_o)u(x, t_n')dx. \quad (32)$$

We will also assume that the voltage in the normal rhythm

$$v_0 = \int g(x - x_o)u_0(x, \tau)dx \quad (33)$$

is unknown and needs to be determined. In principle, τ can be chosen independently for observation and control; in this paper we choose τ to be the same, again for simplicity. The performance of the control scheme can be improved by lifting this restriction.

From the definition of δz and (20) we have

$$v^n = v_0 + \sum_{i=1}^{\infty} C_i \xi_i^n, \quad (34)$$

where $C_i = \langle e_i(\tau), \hat{u}g(x - x_o) \rangle \approx e_i^u(x_o, \tau)$. Truncating (34) to m leading modes and rewriting it in matrix form yields a relationship between the measurements (outputs) and the mode amplitudes retained in the Galerkin truncation (26),

$$v^n = v_0 + C\xi^n, \quad (35)$$

where $C = [C_1, \dots, C_m]$.

Once again, (34) allows an important interpretation. Whenever $C_i \approx e_i^u(x_o, \tau) = 0$, the measured voltage becomes

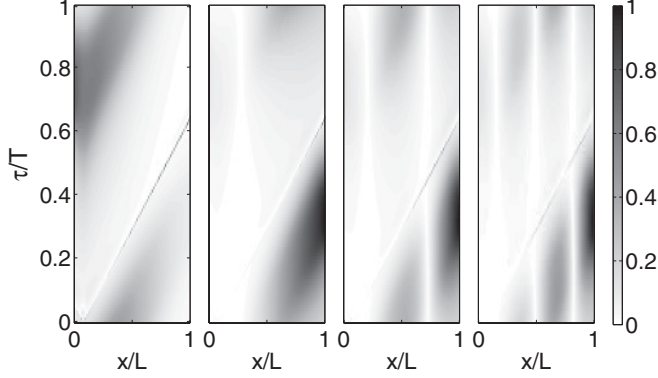


FIG. 9. Observability $|e_i^u(x, \tau)|$ of the four leading modes for $L = 3$ cm and $T = 185$ ms. From left to right, $i = 1, 2, 3, 4$, respectively.

independent of the mode amplitude ξ_i^n (mode i becomes *unobservable*). This means that ξ_i^n cannot be determined regardless of the procedure used to extract it. If the unobservable mode is unstable, we cannot expect the feedback to suppress it either, so that observability of unstable modes imposes additional restrictions on the timing τ of voltage recordings and the position x_o of the recording electrode. From the observability standpoint, the optimal choice of τ corresponds to the range where $|e_i^u(x_p, \tau)|$ are near maximal values at least for all unstable modes (and preferably for all the modes included in the Galerkin truncation).

Unlike the case of controllability, this optimal range is fiber-length dependent: We find $0.5T \lesssim \tau \lesssim 0.9T$ for $L = 1$ cm (see Fig. 5), but $0.8T \lesssim \tau \lesssim 1.2T$ for $L = 2$ cm (see Fig. 8). On the other hand, the optimal spatial location for the recording electrode, regardless of fiber length, is found to be near the far end of the fiber, $0.9L \lesssim x_o \lesssim L$. Interestingly, for longer fibers (see, e.g., Fig. 9 for $L = 3$ cm), the leading mode gradually loses observability at the far end of the fiber, but remains observable at $x_o = x_p$. This means that voltage recordings from two electrodes are required for complete observability: the pacing electrode and a recording electrode at the far end of the fiber.

With a proper choice of x_o and τ to satisfy the observability conditions, we can follow the standard procedure [27] to reconstruct the mode amplitudes ξ_i^n from a series of voltage recordings v^n, v^{n-1}, \dots . In the linear approximation, the actual dynamics of the mode amplitudes is given by (30) or, written in a slightly different form,

$$\begin{pmatrix} \xi^{n+1} \\ v_0 \end{pmatrix} = \begin{pmatrix} A & 0 \\ 0 & 1 \end{pmatrix} \begin{pmatrix} \xi^n \\ v_0 \end{pmatrix} + \begin{pmatrix} B' \\ 0 \end{pmatrix} Q^n. \quad (36)$$

Let us construct a corrected model for the estimates $\xi^n = [\xi_1^n, \dots, \xi_m^n]^\dagger$ and w^n of ξ^n and v_0 , respectively:

$$\begin{pmatrix} \xi^{n+1} \\ w^{n+1} \end{pmatrix} = \begin{pmatrix} A & 0 \\ 0 & 1 \end{pmatrix} \begin{pmatrix} \xi^n \\ w^n \end{pmatrix} + \begin{pmatrix} B' \\ 0 \end{pmatrix} Q^n + H \left[v^n - (C 1) \begin{pmatrix} \xi^n \\ w^n \end{pmatrix} \right], \quad (37)$$

where the additional terms on the right-hand side represent corrections to the mode amplitudes due to differences in the output of the model and the experimental system. Subtracting

(36) from (37) and using (35) we arrive at the equation for the differences $\delta\xi^n = \xi^n - \xi^n$ and $\delta w^n = w^n - v_0$:

$$\begin{pmatrix} \delta\xi^{n+1} \\ \delta w^{n+1} \end{pmatrix} = \left[\begin{pmatrix} A & 0 \\ 0 & 1 \end{pmatrix} - H(C 1) \right] \begin{pmatrix} \delta\xi^n \\ \delta w^n \end{pmatrix}. \quad (38)$$

It is easy to ensure that $\delta\xi^n \rightarrow 0$ and $\delta w^n \rightarrow 0$, so that $\xi^n \rightarrow \xi^n$ and $w^n \rightarrow v_0$, for $n \rightarrow \infty$ by a proper choice of the observer gain H which makes the matrix on the right-hand side of (38) stable. Just as the feedback gain K , we also computed H using dlqr.

The convergence of the estimator (37) crucially depends on a proper choice of the initial estimate ξ^1 and w^1 . We found that, for the pacing protocol used here (see Sec. III), the leading mode is initially dominant, $|\xi_1^1| \gg |\xi_i^1|, i = 2, 3, \dots, m$. Based on this observation, we set $\xi_i^1 = 0, i = 2, 3, \dots, m$. To avoid exciting the subleading modes before the initial estimates of ξ_1^1 and w^1 have been obtained, we did not apply feedback during the first pacing interval. Hence, from (34) and (28) with $Q^1 = 0$, we find that w^1 and ξ_1^1 should satisfy the following system of equations:

$$v^1 = w^1 + C_1 \xi_1^1, \quad (39a)$$

$$v^2 = w^1 + \lambda_1 C_1 \xi_1^1. \quad (39b)$$

Replacing the controller (31) with

$$Q^n = -K \xi^n, \quad (40)$$

and combining (40) with the observer (37) yields a single-input single-output (SISO) control procedure (known as a *compensator*) that could easily be applied in an experimental setting. Below we illustrate its performance using the full nonlinear model of the fiber represented by the partial differential equation (3). In particular, we investigate the effects of mode truncation and the placement of the recording electrode.

VI. RESULTS AND CONCLUSIONS

In order to directly compare the performance of the compensator with PIA control we used the same electrode for pacing and feedback and followed the protocol introduced in Ref. [9]. As we discussed in Sec. III, PIA fails to maintain normal rhythm whenever a second unstable mode appears. The failure of PIA control is illustrated in Fig. 10(a), which shows the evolution of the two unstable modes for $L = 1$ cm. Although initially quite small, the amplitude of the subleading mode grows exponentially with the rate close to λ_2 , as expected due to its weak controllability. The leading mode, on the other hand, is controllable and hence is initially suppressed by feedback. However, its dynamics is slaved to that of the growing subleading mode through the nonlinear terms in the ionic model. Once the amplitude of the subleading mode becomes sufficiently large, the leading mode also starts to grow as feedback is overpowered by mode coupling.

In contrast, the compensator succeeds even when additional unstable modes appear, as Fig. 3 shows. For instance, for $L = 1$ cm, controllability and observability conditions can be satisfied by placing the recording electrode in the optimal location $x_o = 0.9$ cm and choosing $\tau = 0.54T$. In this case truncation to $m = 2$ modes is sufficient to suppress alternans

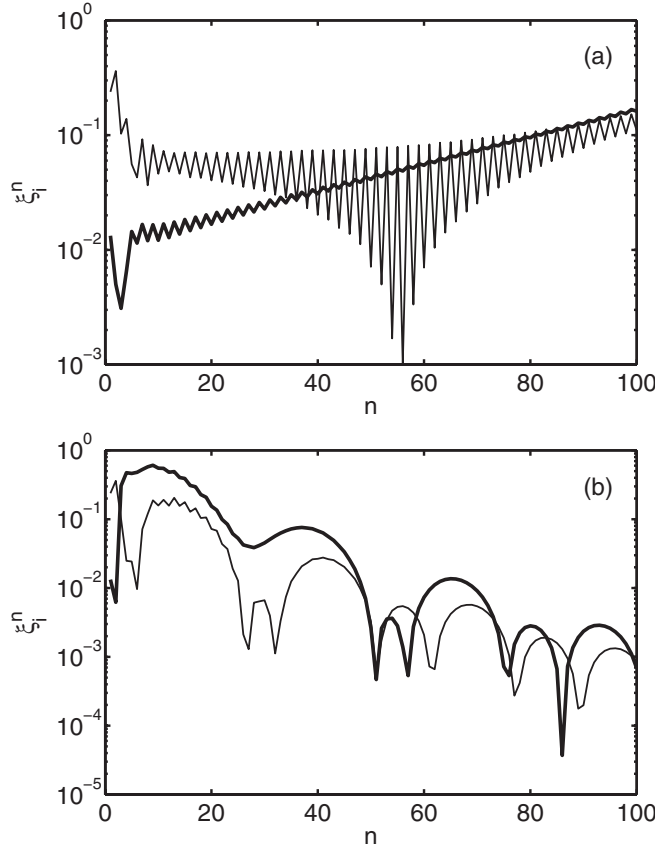


FIG. 10. Mode amplitudes ξ_1^n (thin line) and ξ_2^n (thick line) under (a) PIA and (b) model-based control for $L = 1$ cm and $T = 205$ ms. In both cases the initial condition is the normal rhythm for $T = 210$ ms and control is turned on at $n = 1$.

for any T , including the values where PIA control fails, as illustrated by Fig. 10(b). On the other hand, if the pacing electrode is also used for observation, $x_o = x_c = 0.25$ cm, the compensator performance deteriorates significantly when the same two-mode truncation is used. Predictably, it is the observer part which starts to fail in the latter case. As a quick comparison of Figs. 11(a) and 11(b) shows, for $x_o = 0.25$ cm the estimates of the mode amplitudes differ significantly from the actual values, while for $x_o = 0.9$ cm the estimates remain fairly accurate.

The fundamental problem here is the decreased observability of both unstable modes at $x_o = 0.25$ cm (see Fig. 5), which requires the use of a large observer gain H . The latter, in turn, reduces the region of validity of the linear approximation (37). The protocol used here produces initial perturbations that, in fact, are not small to begin with. The initial condition \mathbf{z}_i (normal rhythm at $T = 210$ ms) deviates quite significantly from the target state \mathbf{z}_0 (normal rhythm at $T = 205$ ms). As Fig. 8 shows, the voltage $u(x_p, t)$ changes from its minimal, to its maximal, value in ~ 5 ms following the pacing impulse, placing the perturbation in the nonlinear regime.

The nonlinear origin of the observer failure can be confirmed by decreasing the initial deviation from the target state. For instance, reducing $\mathbf{z}_i - \mathbf{z}_0$ by a factor of 10 considerably improves the accuracy of the estimates, as Fig. 11(d) illustrates. A partial solution to the problem of weak observability is

provided by increasing the truncation order of the compensator to include a number of weakly stable modes, in addition to the unstable ones. This has an effect of expanding the region of validity of the linear approximation (37). For instance, truncation to $m = 4$ modes produces radically more accurate estimates of the mode amplitudes [shown in Fig. 11(c)] for the same initial disturbance as in Figs. 11(a) and 11(b), restoring the efficiency of the compensator. However, for $L \gtrsim 1.5$ cm the compensator fails for any truncation order, if the same electrode is used for pacing, control, and recording.

Although the range of parameters for which alternans can be suppressed is extended significantly by replacing PIA with compensator control described here, even further improvement is possible with some modifications. While the maxima of $|f_i^u(x_c, \tau)|$ are achieved for the same value of τ regardless of the fiber length (this optimum is determined by the local cell dynamics), the maxima of $|e_i^u(x_o, \tau)|$ shift linearly with the fiber length (information propagates away from the pacing and control site with the speed determined by the conduction velocity). For fibers longer than ~ 1 cm, controllability and observability may not be both satisfied for the same value of τ . For instance, for $L = 2$ cm, $|e_i^u(x_o, \tau)|$ are maximal for $\tau \approx T$ when $|f_i^u(x_p, \tau)|$ are near their minima (see Fig. 8), so that τ has to be chosen differently for the controller and the observer.

To illustrate an improvement possible with a more accurate state reconstruction procedure, we note that if the system state is known, $\xi^n = \xi^u$, (40) reduces to (31) and model-based control can suppress alternans for up to $L \approx 2$ cm (see Fig. 3). For even longer fibers the approach based on impulsive feedback fails and *continuous-time* voltage measurement and current feedback are required to suppress alternans. Both are straightforward to implement. For instance, continuous-time feedback can be computed using the model (26) as opposed to (30). Substantial improvements can also be made by changing the protocol to reduce the pacing interval more gradually, instead of making large 5-ms steps, thereby significantly mitigating the nonlinear effects. All of these changes are straightforward to implement, but have not been explored in this paper, whose main focus is on the issues of observability and controllability.

Finally, we should point out that feedback via electric current is not the only way to suppress alternans. It can be argued, especially given the importance of calcium cycling in the emergence of alternans, that control may be more effective when feedback is applied to one of the gating variables (i.e., a , b , or c here) [28]. This can significantly alter both the controllability and the observability properties of the dynamics, potentially increasing the size of the tissue which can be controlled using spatially localized feedback. At the moment, however, it is unclear whether, or how, such feedback can be implemented in practice, so feedback via direct injection of electric current remains the only practically viable choice.

In summary, we have shown that, following a systematic model-based approach, it is possible to design a control procedure that overcomes the limitations of the PIA approach, yet is still simple to implement experimentally. The model-based analysis also allows one to determine how the electrodes should be arranged along the fiber, regardless of the method used to determine the feedback current. Specifically, to achieve controllability, the control electrodes should be placed at the spatial locations where the unstable adjoint eigenfunctions

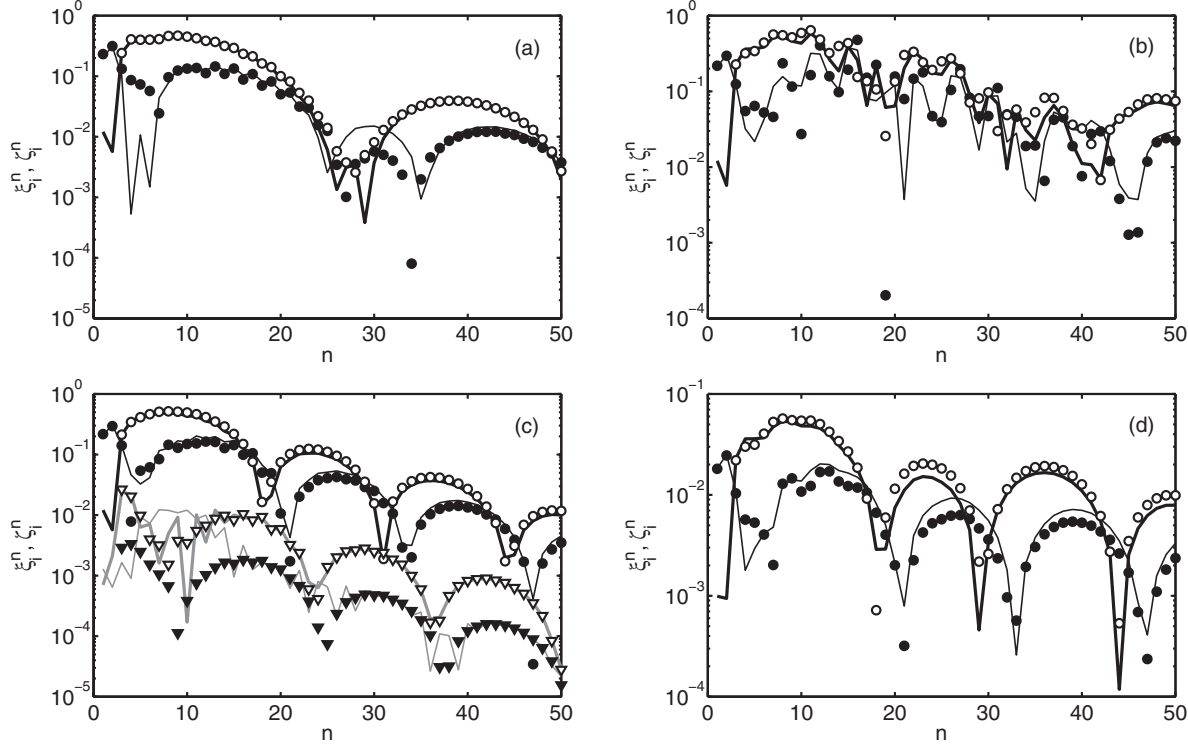


FIG. 11. Mode amplitudes ξ_1^n (thin black line), ξ_2^n (thick black line), ξ_3^n (thin gray line), ξ_4^n (thick gray line) and their estimates ζ_1^n (filled circles), ζ_2^n (open circles), ζ_3^n (filled triangles), ζ_4^n (open triangles) during compensator control for $L = 1$ cm, $T = 205$ ms. (a) $x_o = 0.9$ cm and $m = 2$; (b) $x_o = 0.25$ cm and $m = 2$; (c) $x_o = 0.25$ cm and $m = 4$; (d) same as (b), but with smaller initial disturbance.

$\mathbf{f}_i(x_p, \tau)$ are close to their maxima. This requirement can be satisfied, for instance, by collocating the pacing and control electrodes. Similarly, to achieve observability, the recording electrodes should be placed where the unstable eigenfunctions $\mathbf{e}_i(x_o, \tau)$ are near their maxima. For fibers shorter than ~ 2 cm this can be achieved by placing one recording electrode near the end of the fiber opposite the pacing site. For fibers longer than 2 cm an additional recording electrode is needed to satisfy the observability condition; it can be collocated with the pacing electrode. Both controllability and observability also depend on timing. For instance, PIA control breaks down because, for the particular choice of the feedback timing, subleading modes are rendered uncontrollable. Finally, it should be mentioned that the analysis presented here is applicable to other excitable systems and, in particular, other types of cardiac tissue (e.g., atrial and ventricular muscle), paving the way for clinical applications.

ACKNOWLEDGEMENT

This material is based upon work supported by the National Science Foundation under Grant Nos. 1028133, 0800793, and 1028261.

APPENDIX A: NUMERICAL METHODS

The evolution equation (3) has been solved numerically using the explicit Euler method and finite-difference discretization with $\Delta x = 0.01$ cm and $\Delta t = 0.01$ ms. Additional

details on computing the eigenfunctions and time-periodic solutions are provided below.

1. Calculation of the normal rhythm by a Newton-Krylov method

We start by writing (9) as

$$G[\mathbf{z}_0] - \mathbf{z}_0 = 0. \quad (\text{A1})$$

The problem of finding the root \mathbf{z}_0 defined by (A1) can be solved by Newton's method. In order to find a correction $\delta\mathbf{z}_n$ to an estimate \mathbf{z}_n of \mathbf{z}_0 , we approximate the left-hand side of (A1) by its Taylor series expansion up to first order in $\delta\mathbf{z}_n$,

$$\begin{aligned} 0 &= G[\mathbf{z}_n + \delta\mathbf{z}_n] - \mathbf{z}_n - \delta\mathbf{z}_n \\ &\approx G[\mathbf{z}_n] + J_G|_{\mathbf{z}_n} \delta\mathbf{z}_n - \mathbf{r}_n - \delta\mathbf{z}_n, \end{aligned} \quad (\text{A2})$$

where J_G is the Jacobian of G evaluated at \mathbf{z}_n ,

$$J_G|_{\mathbf{z}_n} \delta\mathbf{z} = \lim_{\epsilon \rightarrow 0} \frac{G[\mathbf{z}_n + \epsilon \delta\mathbf{z}] - G[\mathbf{z}_n]}{\epsilon}. \quad (\text{A3})$$

Rearranging terms in (A2), we obtain

$$(J_G|_{\mathbf{z}_n} - I)\delta\mathbf{z}_n = \mathbf{z}_n - G[\mathbf{z}_n], \quad (\text{A4})$$

where I is the identity operator. (A4) is a linear equation with the function $\delta\mathbf{z}_n$ as the unknown. In order to solve (A4), we discretized it by the method of finite differences on the same (uniform) grid used for the numerical integration of (3), $x_i = (i - 1)\Delta x$, $i = 1, \dots, N$ with $N = L/\Delta x + 1$. Hence, the state vector \mathbf{z} with four elements, each of which is a function of x , $\mathbf{z}(x) = [u(x), a(x), b(x), c(x)]$, becomes a vector of $4N$

elements, $\mathbf{r} = [r_1, \dots, r_{4N}]$,

$$\begin{aligned} [r_1, \dots, r_N] &= [u(x_1), \dots, u(x_N)], \\ [r_{N+1}, \dots, r_{2N}] &= [a(x_1), \dots, a(x_N)], \\ [r_{2N+1}, \dots, r_{3N}] &= [b(x_1), \dots, b(x_N)], \\ [r_{3N+1}, \dots, r_{4N}] &= [c(x_1), \dots, c(x_N)]. \end{aligned} \quad (\text{A5})$$

After discretization, (A4) becomes a $4N \times 4N$ linear system of algebraic equations

$$(J_{\tilde{G}}|_{\mathbf{r}_n} - \tilde{I})\delta\mathbf{r}_n = \mathbf{r}_n - \tilde{G}[\mathbf{r}_n], \quad (\text{A6})$$

where $\delta\mathbf{r}_n$ is the discretized version of $\delta\mathbf{z}_n$, \tilde{G} is the discretized version of G , $J_{\tilde{G}}|_{\mathbf{r}_n}$ is the Jacobian of \tilde{G} , and \tilde{I} is a unit matrix. The result of the operation $\tilde{G}[\mathbf{r}]$ is calculated as the state arrived at by numerically advancing the spatial discretization of (3) from $t = 0$ to $t = T$, with \mathbf{z} as the initial condition.

We solved (A6) by generalized minimal residual method (GMRES) implemented by the Matlab function gmres. In using GMRES we have two alternatives: providing the explicit matrix representation of $J_{\tilde{G}}|_{\mathbf{r}_n}$ or calculating the matrix-vector product $J_{\tilde{G}}|_{\mathbf{r}_n}\delta\mathbf{r}_n$ directly (matrix-free form). For efficiency, we used the matrix-free form based on the finite-difference approximation

$$J_{\tilde{G}}|_{\mathbf{r}_n} \delta\mathbf{r}_n \approx \frac{\tilde{G}[\mathbf{r}_n + \epsilon\delta\mathbf{r}_n] - \tilde{G}[\mathbf{r}_n]}{\epsilon}, \quad (\text{A7})$$

where ϵ was chosen so that $\epsilon\|\delta\mathbf{r}_n\|_1/\|\mathbf{r}_n\|_1 = 10^{-6}$, where $\|\mathbf{r}\|_1 = \max_i |r_i|$.

Provided a sufficiently good initial guess \mathbf{r}_1 is made, the recurrence relation $\mathbf{r}_{n+1} = \mathbf{r}_n + \delta\mathbf{r}_n$, with $\delta\mathbf{r}_n$ given by Eq. (A6), converges toward \mathbf{r}_0 (the discretized version of \mathbf{z}_0). The use of Newton's method, together with the matrix-free form of a Krylov-space linear solver such as GMRES, constitutes what is known as a matrix-free Newton-Krylov method [23].

2. Calculation of the right eigenfunctions of $U(T, 0)$

We approximated $U(T, 0)$ by its discretization $\tilde{U}(T, 0)$. The eigenvalues λ_i and the (right) eigenfunctions $\mathbf{e}_i(0)$ (we omitted the x dependence to simplify notation) of $\tilde{U}(T, 0)$ were found using the implicitly restarted Arnoldi iteration method [29], implemented by the MATLAB routine eigs. For the sake of efficiency, this method was also applied in its matrix-free form using a routine that calculates the matrix-vector product $\tilde{U}(T, 0)\delta\mathbf{r}$, instead of the explicit matrix representation of $\tilde{U}(T, 0)$. By inverting the order of the linearization of the dynamics and the integration over one period, it follows immediately that $U(T, 0)$ is the same as the Jacobian J_G defined by Eq. (A3), evaluated at \mathbf{z}_0 . This identity gives the procedure for the calculation of the matrix-vector product

$$\tilde{U}(T, 0)\delta\mathbf{r} \approx \frac{\tilde{G}[\mathbf{r}_0 + \epsilon\delta\mathbf{r}] - \tilde{G}[\mathbf{r}_0]}{\epsilon}, \quad (\text{A8})$$

with ϵ chosen as in (A7).

A. Calculation of the left eigenfunctions of $U(T, 0)$

The left eigenfunctions $\mathbf{f}_i(0)$ were computed as the right eigenfunctions of $U^\dagger(T, 0)$ also using the MATLAB routine

eigs in its matrix-free form. We computed the matrix-vector product corresponding to $U^\dagger(T, 0)\delta\mathbf{z}$ as follows. If Eq. (10), in the absence of control, is integrated in time using explicit Euler method, we obtain

$$U(T, 0) \approx \prod_{i=0}^{M-1} [1 + \Delta t J_N(t_i)], \quad (\text{A9})$$

where $t_i = i\Delta t$ and $M = T/\Delta t$. Taking the adjoint of both sides of (A9) and multiplying by $\delta\mathbf{z}$ yields

$$U^\dagger(T, 0)\delta\mathbf{z} \approx \prod_{i=M-1}^0 [1 + \Delta t J_N^\dagger(t_i)]\delta\mathbf{z}. \quad (\text{A10})$$

For a uniform mesh, the discretization of $J_N^\dagger(t_i)$ is simply the transpose conjugate of the discretization of $J_N(t_i)$.

APPENDIX B: LEFT AND RIGHT EIGENFUNCTIONS ON THE POINCARÉ SECTION

Here we derive the expressions for the left and right eigenfunctions of the evolution operator $U(\tau + T, \tau)$ which defines the stroboscopic map (13) with $0 < \tau < T$.

1. Right eigenfunctions

Taking the special case $\tau = 0$ of (14) and omitting the x dependence to simplify notation yields

$$U(T, 0)\mathbf{e}_i(0) = \lambda_i \mathbf{e}_i(0). \quad (\text{B1})$$

Multiplying both sides of (B1) by $U(\tau + T, T)$ we obtain

$$U(\tau + T, 0)\mathbf{e}_i(0) = \lambda_i U(\tau + T, T)\mathbf{e}_i(0), \quad (\text{B2})$$

where we have used the property

$$U(t_f, t_i) = U(t_f, t') U(t', t_i) \quad (\text{B3})$$

of the evolution operator with $t' = T$. Applying this property to the left-hand side of (B2) with $t' = \tau$ and using (12) on the right-hand side, we obtain

$$U(\tau + T, \tau) U(\tau, 0)\mathbf{e}_i(0) = \lambda_i U(\tau, 0)\mathbf{e}_i(0). \quad (\text{B4})$$

Comparing (B4) with (14) yields (15).

2. Left eigenfunctions

From (B3) it follows that

$$U^\dagger(t_f, t_i) = U^\dagger(t', t_i) U^\dagger(t_f, t'). \quad (\text{B5})$$

Using (B5), the operator on the left-hand side of

$$U^\dagger(T, 0)\mathbf{f}_i(0) = \lambda_i^* \mathbf{f}_i(0) \quad (\text{B6})$$

can be written as

$$U^\dagger(T, 0) = U^\dagger(\tau, 0) U^\dagger(T, \tau). \quad (\text{B7})$$

Multiplying (B6) by $U^\dagger(T, \tau)$ and using (B7) we get

$$U^\dagger(T, \tau) U^\dagger(\tau, 0) U^\dagger(T, \tau) \mathbf{f}_i(0) = \lambda_i^* U^\dagger(T, \tau) \mathbf{f}_i(0). \quad (\text{B8})$$

Using (B5) and (12), the first two factors on the left-hand side of (B8) can be written as

$$U^\dagger(T, \tau) U^\dagger(\tau, 0) = U^\dagger(\tau + T, \tau), \quad (\text{B9})$$

hence (B8) reduces to

$$U^\dagger(\tau + T, \tau) U^\dagger(T, \tau) \mathbf{f}_i(0) = \lambda_i^* U^\dagger(T, \tau) \mathbf{f}_i(0). \quad (\text{B10})$$

Comparing (B10) with (17) yields

$$\mathbf{f}_i(\tau) = \alpha_i U^\dagger(T, \tau) \mathbf{f}_i(0), \quad (\text{B11})$$

where α_i is a constant. From (B11) for $\tau = 0$ it follows that $\alpha_i = (\lambda_i^*)^{-1}$, which proves (18).

- [1] G. R. Mines, *J. Physiol. (London)* **46**, 349 (1913).
- [2] M. R. Guevara, G. Ward, A. Shrier, and L. Glass, in *Computers in Cardiology 1984* (IEEE Computer Society, Long Beach, CA, 1984), p. 167.
- [3] J. M. Pastore, S. D. Girouard, K. R. Laurita, F. G. Akar, and D. S. Rosenbaum, *Circulation* **99**, 1385 (1999).
- [4] M. A. Watanabe, F. H. Fenton, S. J. Evans, H. M. Hastings, and A. Karma, *J. Cardiovasc. Electrophysiol.* **12**, 196 (2001).
- [5] S. M. Narayan, *J. Am. Coll. Cardiol.* **47**, 269 (2006).
- [6] E. M. Cherry and F. H. Fenton, *New J. Phys.* **10**, 125016 (2008).
- [7] K. Pyragas, *Phys. Lett. A* **170**, 421 (1992).
- [8] G. M. Hall and D. J. Gauthier, *Phys. Rev. Lett.* **88**, 198102 (2002).
- [9] B. Echebarria and A. Karma, *Chaos* **12**, 923 (2002).
- [10] D. J. Christini, M. L. Riccio, C. A. Culianu, J. J. Fox, A. Karma, and R. F. Gilmour Jr., *Phys. Rev. Lett.* **96**, 104101 (2006).
- [11] W. J. Rappel, F. Fenton, and A. Karma, *Phys. Rev. Lett.* **83**, 456 (1999).
- [12] D. Noble, *J. Physiol.* **160**, 317 (1962).
- [13] D. Di Francesco and D. Noble, *Philos. Trans. R. Soc. London B* **307**, 353 (1985).
- [14] O. V. Aslanidi, P. Stewart, M. R. Boyett, and H. G. Zhang, *Biophys. J.* **97**, 20 (2009).
- [15] K. J. Sampson, V. Iyer, A. R. Marks, and R. S. Kass, *J. Physiol.* **588**, 2643 (2010).
- [16] J. B. Nolasco and R. W. Dahlen, *J. Appl. Physiol.* **25**, 191 (1968).
- [17] Z. Qu, A. Garfinkel, P.-S. Chen, and J. N. Weiss, *Circulation* **102**, 1664 (2000).
- [18] F. H. Fenton, E. M. Cherry, H. M. Hastings, and S. J. Evans, *Chaos* **12**, 852 (2002).
- [19] E. M. Cherry and F. H. Fenton, *Am. J. Physiol.* **286**, H2332 (2004).
- [20] Y. Nakaya, A. Varro, V. Elharrar, and B. Surawicz, *J. Cardiovasc. Pharm.* **14**, 908 (1989).
- [21] D. Alexandre and N. F. Otani, *Phys. Rev. E* **70**, 061903 (2004).
- [22] A. Garzón, R. O. Grigoriev, and F. H. Fenton, *Phys. Rev. E* **80**, 021932 (2009).
- [23] D. A. Knoll and D. E. Keyes, *J. Comput. Phys.* **193**, 357 (2004).
- [24] R. B. Lehoucq and D. C. Sorensen, *SIAM J. Matrix Anal. Appl.* **17**, 789 (1996).
- [25] M. Li and N. F. Otani, *Ann. Biomed. Eng.* **32**, 784 (2004).
- [26] P. Dorato, C. T. Abdallah, and V. Cerone, *Linear Quadratic Control* (Krieger, Melbourne, FL, 2000).
- [27] S. H. Zak, *Systems and Control* (Oxford University Press, New York, 2003).
- [28] L. M. Muñoz, J. F. Stockton, and N. F. Otani, *Ann. Biomed. Eng.* **38**, 2865 (2010).
- [29] R. B. Lehoucq, D. C. Sorensen, and C. Yang, *ARPACK Users' Guide: Solution of Large-Scale Eigenvalue Problems with Implicitly Restarted Arnoldi Methods* (SIAM, Philadelphia, 1998).